Study of xenon $4d$, $5p$, and $5s$ photoionization in the shape-resonance region using spin-resolved electron spectroscopy

G. Snell,[1,2,*] U. Hergenhahn,[2] N. Müller,[1] M. Drescher,[1] J. Viefhaus,[2] U. Becker,[2] and U. Heinzmann[1]
[1]*Universität Bielefeld, 33501 Bielefeld, Germany*
[2]*Fritz-Haber-Institut der Max-Planck-Gesellschaft, 14195 Berlin, Germany*
(Received 31 August 2000; published 13 February 2001)

Photoionization of Xe atoms is investigated close to the maximum of the $4d$ shape resonance by means of spin-resolved photoelectron spectroscopy. Using circularly and linearly polarized synchrotron radiation of 93.8-eV energy, we investigate the photoionization processes of the $5p$, $5s$, and $4d$ shells. By combination of earlier data for the partial and differential cross sections with our measurements, we are able to perform a complete characterization of the Xe $4d$ photoionization process, i.e., we can determine all the relativistic dipole matrix elements. Comparison with different theoretical calculations shows the importance of relaxation effects at this photon energy.

DOI: 10.1103/PhysRevA.63.032712 PACS number(s): 32.80.Hd, 32.80.Fb

I. INTRODUCTION

The $4d$ photoionization process of xenon has been a showcase subject of inner-shell ionization for more than three decades, and a benchmark experiment for theoretical models. This is because the photoionization of this subshell exhibits strong electron correlation effects [1] in addition to pronounced single-particle phenomena [2] such as shape resonances and Cooper minima [3,4], which makes it difficult to distinguish between different origins for a certain behavior of the partial cross section, as well as other quantities amenable to photoionization studies. Despite the large number of partial cross-section and angular distribution studies [5], only a very few experiments were able to derive information beyond these quantities in order to give a complete description of Xe $4d$ photoionization in terms of the dipole matrix elements [6–9].

A complete characterization of a photoionization process means that all quantities which describe the photon-atom interaction quantum mechanically are determined. This notion is obviously model dependent. Experiments on valence shells were performed using gas discharge lamps and synchrotron radiation up to a photon energy of approximately 40 eV [10]. The first ''complete experiment'' on an inner shell described Mg $2p$ photoionization within the LS-coupling approximation with three experimental parameters [11]. For inner-shell processes, it seems more appropriate to start from a relativistic description of the process, that is, photoionization amplitudes are characterized by quantum numbers l and j of the outgoing electron, and J_i and J_f of the initial and final ionic states. Within the relativistic model the Xe $4d$ inner-shell photoionization process was characterized by Kämmerling and co-workers [6,7] and Schaphorst *et al.* [8] using electron-electron coincidence spectroscopy. As an alternative approach, in the present paper we describe a detailed investigation of Xe $4d$ photoionization in the framework of a relativistic model, by means of spin- and angle-resolved electron spectroscopy.

In this work, we report on spin polarization measurements of Xe $5s$, $5p$, and $4d$ photoelectrons using circularly and linearly polarized synchrotron radiation of 93.8-eV energy. By critically analyzing the process of data extraction from our measured quantities and values obtained from the literature, we are able to uniquely determine relativistic dipole matrix element amplitudes and phase differences together with a calibration for the polarization sensitivity S_{eff} and the instrumental asymmetry of our electron polarimeter. Since this process of data analysis is crucial to our results, it will be described in some detail. Results will be compared with theoretical work using several variants of the random-phase-approximation (RPA) theory, and explicit forms for all photoionization observables considered in this work in terms of dipole amplitudes and phase differences are given in the Appendix.

A common feature among all experiments (including the present one) which gives a complete description of an inner-shell photoionization process is that, in addition to measurements on the photoelectron, information about the photoion is used. The polarization of the photoion is obtained from angular distribution and spin polarization measurements of Auger electrons, which are emitted during the decay of the inner-shell hole. This is in accordance with a recent finding by Schmidtke *et al.* [12], that a complete set of relativistic dipole matrix elements cannot be obtained solely from the properties of the photoelectron.

Highly differential measurements, which are needed for a complete characterization of a photoionization process, are technically difficult to perform on atomic inner shells for several reasons. In general, photoionization cross sections decrease with increasing photon energy [5]. The measurement of the spin polarization of electrons utilizing Mott-scattering results in a decrease of the electron intensity by 2–3 orders of magnitude [13]. Coincidence techniques are also technically demanding, and often result in low count-rates. Furthermore, circularly polarized radiation has to be used, otherwise two of the three components of the photo-

*Present address: Lawrence Berkeley National Laboratory, University of California, Berkeley, CA 94720.

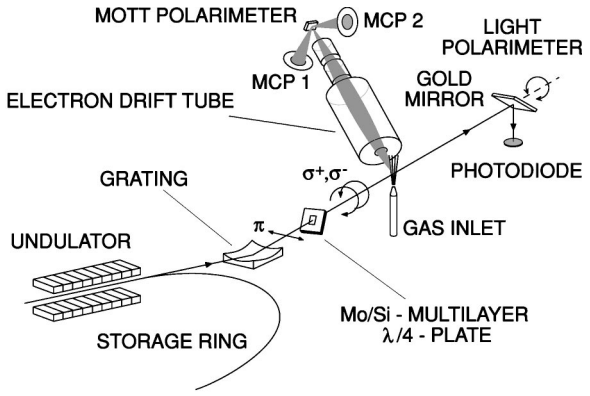

FIG. 1. Experimental setup.

electron spin polarization vector are zero (cf. Sec. III).

These facts made spin-resolved electron spectroscopy on inner shells of free atoms practically impossible until recently. The development of new sources for high intensity, circularly polarized synchrotron radiation, such as the helical undulator of the European Synchrotron Radiation Facility (ESRF) storage ring [14,15], in combination with a very efficient spectrometer system [16], allowed one to overcome the problem of low electron intensity. We performed spin polarization measurements of Xe $3d$ photoelectrons and Xe MNN Auger electrons at a 834.5-eV photon energy at the ESRF [17]. Since no source with suitable polarization characteristics was available to us in the extended x-ray ultraviolet energy range, we used a transmission multilayer acting as a quarterwave plate [18,19] to convert linearly polarized undulator radiation into circularly polarized light. We could achieve a high degree of circular polarization with a reasonable light intensity. The same experimental setup as in the present paper, including the transmission multilayer, was recently used for a spin-resolved study of Xe $N_{4,5}O_{2,3}O_{2,3}$ Auger electrons [20].

II. EXPERIMENT

Figure 1 shows the experimental setup. We used the undulator beamlines U1-TGM5 of the BESSY I storage ring (Berlin) and BW3-SX700 of the Hasylab storage ring (Hamburg) as sources of monochromatized synchrotron radiation. Both beamlines provide a high photon flux of approximately 5×10^{12} photons per second per 100 mA ring current (open exit slits, BW3: $E/\Delta E\approx830$; U1: $E/\Delta E\approx300$) [21–24], with a high degree of linear polarization [BW3: $P_{\rm lin}=0.99(1)$; U1: $P_{\rm lin}=0.97(2)$]. For measurements utilizing circularly polarized radiation, a Mo/Si transmission multilayer (50 bilayers, $d=9$ nm, working range 93 ± 5 eV) was used to convert the incoming linearly polarized light. The photon flux of the circularly polarized radiation was determined to be approximately 10^{11} photons/(s 100 mA) in the interaction region. The helicity of the outgoing beam was changed by rotating the multilayer around the light axis, whereas a variation of the grazing angle was used to tune the multilayer to the desired photon energy.

The light polarization state behind the multilayer was monitored by a Rabinovitch-type linear polarization analyzer [25] consisting of a gold mirror and a Si photodiode. This polarimeter itself cannot distinguish between unpolarized and circularly polarized radiation. However, by successively rotating the multilayer and the polarimeter around the light axis, the polarization of the incoming light (i.e., before the multilayer) and the optical properties of the multilayer and the polarimeter could be determined [26,27]. The almost completely linearly polarized undulator beams, in conjunction with a 90° phase shift of the multilayer, resulted in a high degree of circular polarization [BW3: $P_{\rm circ}=0.99(1)$; U1: $P_{\rm circ}=0.97(2)$].

The energy and polarization analysis of the outgoing electrons was performed by a time-of-flight (TOF) spectrometer combined with a spherical Mott polarimeter of the Rice type [28], operated at 45 kV. Due to the substantial loss of signal intensity during Mott scattering, our experiment benefited considerably from the TOF technique's inherent capability of simultaneous acquisition—and in this case additional spin polarization analysis—of all lines in a spectrum. Since for TOF electron spectroscopy a pulsed light source with appropriate timing is essential, the five-bunch mode of the Hasylab storage ring ($\Delta t=192$ ns) and the single-bunch mode of the BESSY storage ring ($\Delta t=208$ ns) were used. The angular acceptance of the spectrometer was approximately $\pm3°$. To increase the energy resolution, different retarding potentials were applied to the spectrometer drift tube (e.g., $U_{\rm ret}=-70.0$ V for the $5p$ lines). The Xe background pressure in the vacuum chamber was approximately 10^{-4} mbar during measurements.

The component of electron spin perpendicular to the scattering plane is given by the backscattered intensities I_1 and I_2 counted in the multichannel plate detectors MCP1 and MCP2 of the Mott polarimeter:

$$P=\frac{A}{S_{\rm eff}} \quad \text{with} \quad A=\frac{I_1-I_2}{I_1+I_2}, \tag{1}$$

where A is the backscattering asymmetry and $S_{\rm eff}$ (the Sherman function) the polarization sensitivity of the polarimeter. By measuring the spin polarization of the Xe $5p_{1/2}$ photoline with linearly and circularly polarized light (cf. Sec. IV B), the polarization sensitivity was determined to be $S_{\rm eff}=-0.20(3)$.

Instrumental asymmetries of the Mott polarimeter, which can arise, for example, through different detection efficiencies of the MCP's, can be easily eliminated if the sign of the measured spin polarization can be reversed. For this reason successive measurements with positive and negative light helicities were carried out, changing the polarization approximately every 20 min. From the four intensities I_1^+, I_1^-, I_2^+, and I_2^- obtained this way, the electron spin polarization was determined by

$$P=\frac{1}{S_{\rm eff}}\frac{\sqrt{I_1^+I_2^-}-\sqrt{I_1^-I_2^+}}{\sqrt{I_1^+I_2^-}+\sqrt{I_1^-I_2^+}}. \tag{2}$$

For measurements with linearly polarized light, several other methods had to be used to eliminate instrumental asymme-

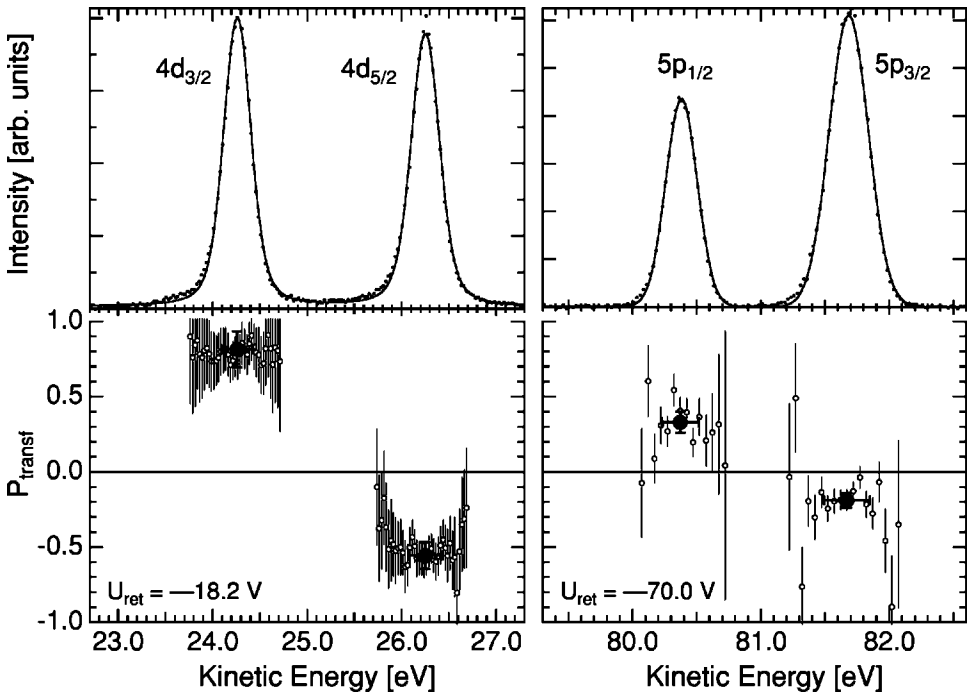

FIG. 2. Xe 4*d* and 5*p* photolines after ionization by circularly polarized 93.8 eV photons. (Top panels) Intensity spectra with fitted Voigt (4*d*) and Gaussian (5*p*) profiles. (Bottom panels) ○, measured spin polarization P_{transf} across the spectra evaluated for each 25-meV (4*d*) and 50-meV (5*p*) kinetic-energy interval of the intensity spectrum; ●, spin polarization of the individual lines evaluated from the areas of the fitted profiles. The vertical error bars include both the statistical and systematic uncertainties. The horizontal bars indicate the FWHM linewidths emerging from the fit.

tries, because then the sign of the electron spin polarization cannot be changed easily. In some cases the instrumental asymmetry was derived from measurements with circularly polarized radiation, which were performed directly before or after the measurements with linearly polarized light. In another approach unpolarized photolines, such as He 1*s* and Xe 5*s*, were used for calibration (cf. Sec. IV A). As a third method we used the fact that when the spin-orbit splitting in the ionic core is neglected the spin polarization of the ''unresolved'' photoline (e.g., 5*p*) vanishes. The last two methods could be used without additional measurements, because in a TOF electron spectrum all lines are present at the same time. For all data presented in this paper at least two of the aforementioned techniques were used to eliminate the instrumental asymmetries for a given line. The results always agreed very well. The possibility to determine the polarization sensitivity and the instrumental asymmetry from the same measurement or measurements very similar to the actual measurement is another distinct advantage of the TOF-Mott spectrometer system, which greatly increased the accuracy and reliability of the results.

During a measurement with our spectrometer, I_1 and I_2 correspond to two time-of-flight electron spectra which are accumulated simultaneously, one in each multichannel plate detector MCP1 and MCP2 of the Mott polarimeter (Fig. 1). Subsequent measurements with positive and negative light helicities yield four electron spectra of the same subject: I_1^+, I_1^-, I_2^+, and I_2^-. The sum of these four spectra, which corresponds to a non-spin-resolved electron spectrum, is displayed in the top panels of Fig. 2 for the 5*p* and 4*d* photolines. Inserting time-of-flight electron spectra into Eq. (1) or (2), for measurements with linearly or circularly polarized radiation, respectively, the spin polarization of every channel of the spectrum (i.e., of all lines and structures) can be obtained. After conversion of the spectra from time of flight (ns) to kinetic energy (eV), this corresponds to a spin polarization for certain kinetic-energy intervals. The results of this ''channel-oriented'' analysis of the 4*d* and 5*p* photolines are plotted in the lower panels of Fig. 2 as open circles.

In order to obtain the spin polarization of the different lines in the spectrum, their intensities have to be determined. This was done in most cases by fitting the spectra with Gaussian or Voigt profiles. Equivalent fit curves of the non-spin-resolved spectra are included in the top panels of Fig. 2. For several measurements the peak areas were determined simply by adding up all the counted events within a line while subtracting a constant background which originates from the dark counts of the detectors. In the lower panels of Fig. 2 the spin polarization results, obtained by circularly polarized radiation, of this line-oriented analysis are shown as closed circles. Comparing the two methods of analysis, we find good agreement for all lines. The error bars of the spin polarization values presented in Fig. 2 and Tables II, III, and V include both the statistical and systematical uncertainties. The angular distribution measurements presented in this paper were performed at the Hasylab storage ring running in a double-bunch mode, using a rotatable vacuum chamber equipped with two 45-cm-long TOF spectrometers [5].

TABLE I. Components of the electron spin polarization in the coordinate system of the electron for arbitrarily polarized radiation for different emission geometries. The measurements in this paper were performed at $(\theta,\phi)=(90°,135°)$; $\phi=135°$ and $\phi=-45°$ are equivalent.

(θ,ϕ)	P_x	P_y	P_z
$(90°,\pm 45°)$	$\dfrac{\pm 2\xi S_1-\left(A+\dfrac{\alpha}{2}\right)S_3}{1+\dfrac{\beta}{4}(1\pm 3S_2)}$	0	0
$(70,\pm 45°)$	$\dfrac{0.94\left[\pm 2\xi S_1-\left(A+\dfrac{\alpha}{2}\right)S_3\right]}{1+\dfrac{\beta}{2}(0.32\pm 1.32S_2)}$	$\dfrac{0.32[2\xi(1\pm S_2)]}{1+\dfrac{\beta}{2}(0.32\pm 1.32S_2)}$	$\dfrac{0.34(A-\alpha)S_3}{1+\dfrac{\beta}{2}(0.32\pm 1.32S_2)}$
$(\theta_m,\pm 45°)$	$\sqrt{\dfrac{2}{3}}\dfrac{\pm 2\xi S_1-\left(A+\dfrac{\alpha}{2}\right)S_3}{1\pm\dfrac{\beta}{2}S_2}$	$\dfrac{\sqrt{2}}{3}\dfrac{2\xi(1\pm S_2)}{1\pm\dfrac{\beta}{2}S_2}$	$\dfrac{1}{\sqrt{3}}\dfrac{(A-\alpha)S_3}{1\pm\dfrac{\beta}{2}S_2}$

III. THEORETICAL BACKGROUND

The description of the photoionization process within the dipole approximation limits the possible values of the angular momentum of the outgoing photoelectrons according to the selection rules. In the case of rare-gas atoms the electron angular momentum j can have the values $j=J_{\rm ion}-1$, $J_{\rm ion}$, and $J_{\rm ion}+1$, with $J_{\rm ion}$ being the total angular momentum of the remaining photoion. Transitions to each of these final states is described by a complex reduced matrix element $De^{i\delta}$ with amplitude D and phase δ. In a quantum mechanically complete experiment all three matrix elements must be determined, i.e., three amplitudes D_-, D_0, and D_+ and two phase differences δ_{-0} and δ_{0+}. This requires the measurement of at least five *independent* quantities.

The geometry of the photoionization process is shown in Fig. 3. The light propagates along the Z axis of the laboratory XYZ frame, whereas the X axis lies in the horizontal plane of the storage ring. The emitted electrons propagate along the z axis of the electron coordinate system xyz. The z and Z axes span the reaction plane.

Photoelectrons are usually spin polarized due to the spin-orbit interaction in the final ionic state (assuming that the splitting can be resolved) and in the continuum for the outgoing electron waves [29]. For our experimental geometry it is convenient to describe the electron-spin polarization in the electron frame xyz. In case of arbitrarily polarized radiation the three components P_x, P_y, and P_z of the spin polarization vector and the differential cross section are given by [30]

$$\frac{d\sigma}{d\Omega}(\theta,\phi)=\frac{\sigma}{4\pi}F(\theta,\phi), \tag{3}$$

$$P_x(\theta,\phi)=[2\xi(S_1\sin 2\phi-S_2\cos 2\phi) -(A+\alpha/2)S_3]\sin\theta/F(\theta,\phi), \tag{4}$$

$$P_y(\theta,\phi)=2\xi(1+S_1\cos 2\phi+S_2\sin 2\phi) \times\sin\theta\cos\theta/F(\theta,\phi), \tag{5}$$

$$P_z(\theta,\phi)=(A-\alpha)S_3\cos\theta/F(\theta,\phi), \tag{6}$$

with

$$F(\theta,\phi)=1-\frac{\beta}{2}\left[P_2(\cos\theta) -\frac{3}{2}(S_1\cos 2\phi+S_2\sin 2\phi)\sin^2\theta\right]. \tag{7}$$

A, α, ξ, and β are the so-called dynamical parameters.[1] S_1, S_2 and S_3 are the normalized Stokes parameters which describe the polarization of the light[2] [31]. The degree of linear polarization is given by $P_{\rm lin}=\sqrt{S_1^2+S_2^2}$. A positive S_3 denotes light with positive helicity, and is called left-handed circular polarization in classical optics [31]. P_x and P_y are perpendicular to the electron propagation direction, and are called transversal components of the spin polarization vector, whereas P_z is called the longitudinal component. β is the angular anisotropy parameter.

Table I gives the spin polarization components for three different directions of electron emission, calculated by Eqs. (4)–(6). Due to the $\cos\theta$ term in Eqs. (5) and (6), P_y and P_z vanish for $\theta=90°$. The measurements described in the present paper were performed at $\theta=90°$ and $\phi=135°$. As the scattering plane incorporating both electron detectors of the Mott polarimeter was located perpendicular to the light beam, the component of the spin polarization vector parallel

[1] In Ref. [30], the parameters $-(A+\alpha/2)$, 2ξ and $(A-\alpha)$ are denoted by ξ, η, and ζ, respectively.

[2] In Eqs. (4) and (5), the sign of S_1 and S_2 was changed with respect to the original equations in Ref. [30].

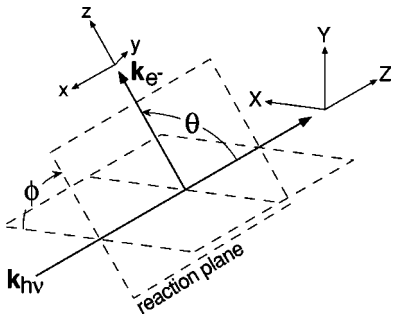

FIG. 3. Geometry of the photoionization process. The light propagates along the *Z* axis, and the electrons along the *z* axis. *XYZ* is the laboratory frame and *xyz* the electron frame.

or antiparallel to the light propagation axis was determined [a positive $P_x(90°,\phi)$ is antiparallel to $\mathbf{k}_{h\nu}$]. The quantity $A(\theta)$, used in previous experiments [32] to describe the transferred spin polarization, relates to P_x in the present geometry by $P_x(90°,\pm 45°)=-A(90°)$ in the absence of linear polarization. A simple interpretation of the equations in Table I can be given using the dynamical parameters.

(i) Using purely circularly polarized light ($S_2=S_1=0$), every component corresponds to a dynamical parameter: P_x, P_y, and P_z to $-(A+\alpha/2)$, ξ, and $(A-\alpha)$, respectively. $-(A+\alpha/2)$ and $(A-\alpha)$ can be measured only if $S_3\neq 0$. The spin polarization in the reaction plane originates from the spin polarization of the photons through a transfer of angular momenta. $-(A+\alpha/2)$ and $(A-\alpha)$ are thus called the parameters of the transferred spin polarization [33,29].

(ii) The component P_y perpendicular to the reaction plane can be measured with light of any polarization or with unpolarized light. The origin of this polarization is a quantum-mechanical interference effect [29], and ξ is often called dynamical polarization.

(iii) Using purely linearly polarized light ($S_2=S_3=0$) the reaction plane is spanned by the electric-field vector and the electron momentum vector and ξ can be determined from P_x.

This last property enabled us to determine $-(A+\alpha/2)$ and ξ, using the same Mott polarimeter in a constant geometry just by changing the light polarization from circular to linear and back. To simplify further discussions we define the following two quantities:

$$P_{\text{transf}}=\frac{P_x(90°,135°)}{S_3}=\frac{-(A+\alpha/2)}{1+\beta/4}, \quad \text{for } S_2=S_1=0, \tag{8}$$

$$P_{\text{dyn}}=\frac{P_x(90°,135°)}{S_1}=\frac{-2\xi}{1+\beta/4}, \quad \text{for } S_2=S_3=0. \tag{9}$$

P_{transf} and P_{dyn} are the two independent quantities which we can measure with the current experimental setup.

Due to kinematic relations, the ranges of the spin polarization parameters are related to the value of the anisotropy parameter β. When β reaches its maximum value 2, all components of the spin polarization must vanish and if $\beta=-1$ the dynamical polarization is zero (Fig. 3 in Ref. [30]).

The partial and differential cross sections and all the dynamical parameters (and their combinations) can be expressed in terms of the dipole matrix elements [30]. The partial cross section corresponds to the sum of the squares of the amplitudes, and is given for closed-shell atoms in the velocity form as

$$\sigma=a_0^2\frac{8\pi^4}{\omega c}\sum_k D_k^2, \tag{10}$$

where a_0 is the Bohr radius in *m*, ω is the photon energy in Hartree, *c* is the speed of light in atomic units (a.u.), and D_k is calculated in atomic units. The relationship between the dipole matrix elements and the measured quantities P_{transf}, P_{dyn}, and β were obtained using Eqs. (8) and (9) and the expressions given in Ref. [30]. For reference purposes they are given in the Appendix for the photoionization of the Xe $4d$, $5s$, and $5p$ subshells.

As described above, for a quantum mechanically complete description of the photoionization process of a closed-shell atom in general, the measurement of at least five independent quantities is necessary. In the present experiment the angular distribution β and the two spin polarization components P_{transf} and P_{dyn} of the photoelectrons can be measured. Together with published values of the partial cross section σ, there are four quantities directly accessible to us. To perform a complete characterization of the photoionization process we have to use further approximations, like the nonrelativistic approach, or we have to determine other photoionization parameters, like the photoion polarization. In some special cases (e.g., $p_{1/2}$ ionization) only three parameters are needed for a complete description of the process.

Inner-shell vacancies, such as a Xe $4d^{-1}$ hole, can relax through a radiationless decay process by emitting Auger electrons. The photoionization process usually leaves the singly charged photoion in a polarized state, i.e., with an uneven population of the magnetic sublevels. Decay of a polarized photoion may lead to an anisotropic angular distribution and also to spin polarization of Auger electrons [34,35]. This opens up the possibility to learn more about the photoionization process from the properties of the Auger electrons. Using the two-step model of Auger decay (for details, see Ref. [36]) the alignment A_{20} and the orientation A_{10} of the primary hole state can be determined from the angular distribution and transferred spin polarization of Auger electrons, respectively. Alignment and orientation are proportional to the electric quadrupole moment and magnetic dipole moment of the photoion, respectively. Similar to the partial cross section σ, alignment and orientation depend only on the squares of the matrix element amplitudes, and are independent of the phase differences. For photoionization processes leading to $^2D_{3/2}$ and $^2D_{5/2}$ final states of the photoion, the expressions for A_{10} and A_{20} in terms of the photoionization amplitudes are given in the Appendix.

IV. RESULTS AND DISCUSSION

A. Xe 5*s* photoionization

The results of our measurements of the spin polarization and angular distribution are shown in Table II. Both P_{transf}

TABLE II. Theoretical and experimental partial cross section σ, spin polarization components P_{transf} and P_{dyn}, and angular anisotropy β for Xe $5s$ photoionization at 93.8 eV.

		Theory[a]	Experiment
$5s^{-1}\,{}^2S_{1/2}$	σ/Mb	0.75	0.41(10)[b]
	P_{transf}	−0.01	0.03(5)
	P_{dyn}	0.01	−0.01(1)
	β	2	1.97(3)

[a]Frozen core RRPA [38].
[b]Reference [39].

and P_{dyn} vanish within the error bars, and β is practically 2 at a 93.8-eV photon energy. These results prove that, at this photon energy the $5s$ photoionization can be described within pure LS coupling, i.e., there is only one outgoing p partial wave and all dynamical parameters have fixed values (cf. the Appendix). Experiments show $\beta=2$ for the s photolines of most rare gases in a broad photon energy range [5]; thus the spin polarization must vanish. This fact was used to determine the instrumental asymmetry of our Mott polarimeter from measurements of the Xe $5s$ and He $1s$ photolines.

A deviation of the anisotropy parameter from $\beta=2$ is a sensitive monitor for the validity of the LS coupling. The strongest deviation from this value was found for the Xe $5s$ line ($\beta\approx 1.3$) in the Cooper minimum of the photoionization cross section at approx. 32-eV photon energy [37].

The only discrepancy between the theory of Ref. [38] and the experimental data is that for the partial cross section, the calculation overestimates s significantly (cf. Table II). A similar situation can also be observed for the Xe $5p$ and $4d$ processes. A possible explanation for these deviations could be that the frozen-core relativistic RPA (RRPA) theory does not take ionization into satellite states into account, which may result in too large a cross section of the main line. A false σ does not necessarily influence the quality of predictions for the other dynamical parameters, because these are relative quantities (cf. the Appendix).

B. Xe $5p$ photoionization

The results of our measurements of the spin polarization and angular distribution are shown in Table III together with other experimental and theoretical data. The different experimental values of the anisotropy parameter β agree very well with each other. There is a good agreement between the RRPA and and RPA with exchange (RPAE) calculations, and also between the experimental and theoretical data, with the exception of the partial cross section which is overestimated by the theory (cf. the discussion above).

For a complete characterization of the process leading to a ${}^2P_{3/2}$ final state, five independent measurements are needed, but only four measured values are available. Since the $5p$ shell is the outermost shell of xenon, it cannot decay by an Auger process, i.e., we cannot obtain further photoionization parameters. The Xe $5p$ photoionization process leading to the ${}^2P_{1/2}$ final state can be described by only three parameters, i.e., a complete characterization of this process with the present experimental setup is possible, since there are four measured quantities. We used this redundancy in the data to determine the polarization sensitivity S_{eff} of our Mott polarimeter.

TABLE III. Theoretical and experimental partial cross section σ, fine-structure intensity ratio ρ $(=\sigma_{3/2}/\sigma_{1/2})$, spin polarization components P_{transf} and P_{dyn}, and angular anisotropy β for Xe $5p$ photoionization at 93.8 eV.

		Theory		Experiment	
		RRPA[a]	RPAE[b]	other	this work
$5p$ Total	σ/Mb	1.60		1.34(2)[c]	
	ρ	1.81		1.73(10)[d]	
	β	1.38	1.30	1.45(7)[e]	$1.42^{+0.08}_{-0.12}$
$5p^{-1}\,{}^2P_{1/2}$	σ/Mb	0.57		0.49(2)[f]	
	P_{transf}	0.30	0.27		0.31(5)
	P_{dyn}	−0.59	−0.54		−0.52(6)
	β	1.39		1.44(10)[d]	
$5p^{-1}\,{}^2P_{3/2}$	σ/Mb	1.03		0.85(2)[f]	
	P_{transf}	−0.14	−0.16[g]		−0.18(4)
	P_{dyn}	0.29	0.31[g]		0.31(5)
	β	1.38		1.46(10)[d]	

[a]Frozen-core relativistic RPA [38].
[b]Frozen-core, nonrelativistic RPA with exchange [55].
[c]Reference [39].
[d]Reference [41].
[e]Reference [42].
[f]Calculated from σ and ρ.
[g]This value was calculated from the ${}^2P_{1/2}$ final state using an experimental branching ratio of 1.73.

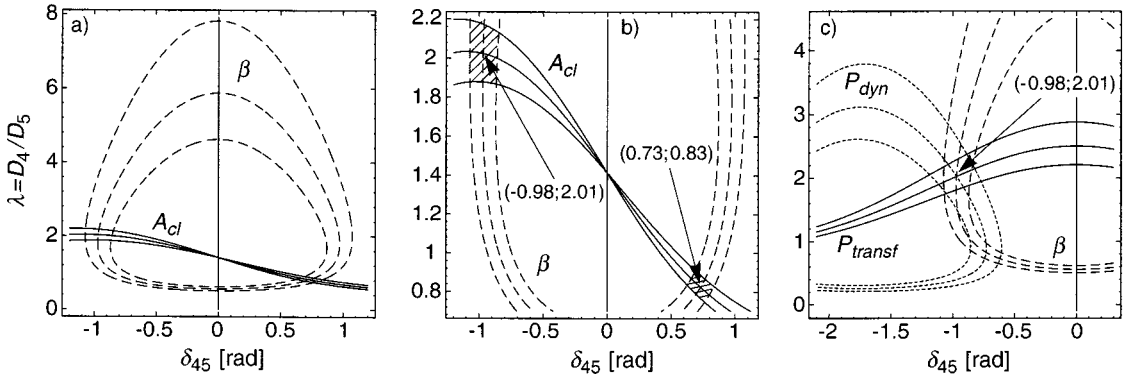

FIG. 4. (a) Two-dimensional contours of values for the amplitude ratio $\lambda = D_4/D_5$ and phase difference δ_{45} of the $5p_{1/2}$ photoionization corresponding to measured values of $\beta = 1.44 \pm 0.10$ (broken lines) and $A_{cl} = -0.65 \pm 0.11$ (solid lines). (b) Enlarged section of (a). (c) Two-dimensional contours of values for λ and δ_{45} resulting from $\beta = 1.44 \pm 0.10$, $P_{\rm dyn} = -0.51 \pm 0.08$, and $P_{\rm transf} = 0.33 \pm 0.06$. In all three figures contours are shown for the measured value and $\pm$ one standard deviation.

Due to the complexity of the equations connecting the matrix elements and the dynamical parameters, and because they contain trigonometric functions (cf. the Appendix), a complicated procedure involving analytical, graphical and numerical methods had to be used to determine the amplitudes D_4 and D_5 and the phase difference δ_{45} [cf. Eq. (A6)] of the $5p_{1/2}$ photoionization from the measurements. The analysis was performed separately for two distinct data sets, one taken at BESSY and one at Hasylab, because the experimental conditions were somewhat different. The procedure shown below is for the BESSY data set.

Using Eqs. (1) and Eqs. (8) and (9), the two spin polarization components $P_{\rm transf}$ and $P_{\rm dyn}$ can be written as

$$P_{\rm transf} = \frac{A_{\rm circ}}{S_3 S_{\rm eff}} \quad \text{and} \quad P_{\rm dyn} = \frac{A_{\rm lin}}{S_1 S_{\rm eff}}, \tag{11}$$

where $A_{\rm circ}$ and $A_{\rm lin}$ are asymmetries measured with circularly and linearly polarized radiation. Since the multilayer quarter-wave plate converted the linear polarization completely into circular polarization, $|S_1| = |S_3|$. This means that the ratio of the spin polarization components is equal to the ratio of the asymmetries. Using the ratio $P_{\rm transf}/P_{\rm dyn}$ instead of $P_{\rm transf}$ and $P_{\rm dyn}$ (together with σ and β) to determine the matrix elements results in values for the amplitudes and phase difference which are independent of the Sherman function $S_{\rm eff}$ and the Stokes parameters S_1 and S_3. Calculating $P_{\rm transf}$ and $P_{\rm dyn}$ from these matrix elements and comparing it with the measured values enabled us to determine $S_{\rm eff}$ of the Mott polarimeter.

We used the experimental data

$$\sigma = 0.49(2)\ \text{Mb}, \quad \beta = 1.44(10), \tag{12}$$

$$P_{\rm transf}/P_{\rm dyn} = A_{\rm circ}/A_{\rm lin} \equiv A_{\rm cl} = -0.65(11)$$

to determine the matrix elements.[3] For a further analysis simplified forms of Eqs. (A10)–(A12) were used, where β and $P_{\rm transf}/P_{\rm dyn}$ are expressed by the ratio of the amplitudes $\lambda = D_4/D_5$ and the phase difference δ_{45}. The partial cross section [Eq. (10)] is given in the present case by

$$\sigma = a_0^2 \frac{8\pi^4}{\omega c}(D_4^2 + D_5^2). \tag{13}$$

(i) First the λ and δ_{45} values were determined which reproduce the experimental data Eq. (12). For this purpose we have plotted $\beta = 1.44 \pm 0.10$ and $A_{\rm cl} = -0.65 \pm 0.11$ in Fig. 4(a). The middle dashed curve represents all possible values of (λ, δ_{45}) pairs compliant with $\beta = 1.44$ through Eq. (A10). The inner and outer dashed curves correspond to $\beta = 1.34$ and 1.54, respectively, and thus define the (λ, δ_{45}) values which are allowed within one standard deviation from the measured value. Similarly, the three solid lines represent $A_{\rm cl} = -0.65$, -0.76, and -0.54. The (λ, δ_{45}) pairs corresponding to both β and $A_{\rm cl}$ are given by the intersections of the dashed and solid lines. As can be seen from Fig. 4(b), there are two sets of solutions:

$$\text{Solution 1:} \quad \lambda = 2.01(16), \quad \delta_{45} = -0.98(10), \tag{14}$$

$$\text{Solution 2:} \quad \lambda = 0.83(9), \quad \delta_{45} = 0.73(11). \tag{15}$$

The shaded areas in Fig. 4(b) were used to assign error bars to λ and δ_{45}.

(ii) In the second step D_4 and D_5 were calculated from σ and λ using Eq. (13):

$$\text{Solution 1:} \quad D_4 = 0.092(3), \quad D_5 = 0.046(3), \quad \delta_{45} = -0.98(10), \tag{16}$$

[3]Note that in Table III the mean values of the two aforementioned data sets are given; thus $A_{\rm cl}$ in Eq. (12) is different from $P_{\rm transf}/P_{\rm dyn}$ of Table III.

$$\text{Solution 2:} \quad D_4 = 0.066(5), \quad D_5 = 0.079(5), \quad \delta_{45} = 0.73(11). \tag{17}$$

Additionally a numerical optimization procedure was performed to find the best set of matrix elements by comparing them to all three measured values at the same time [cf. Eq. (22)]. This process did not change the above values. Both solutions reproduce the experimental data [Eq. (12)] exactly.

(iii) The next step was to extract S_{eff} from the above results. P_{transf} and P_{dyn} can be calculated from Eqs. (A11) and (A12) using Eqs. (16) and (17):

$$\text{Solution 1:} \quad P_{\text{dyn}} = -0.51(6), \quad P_{\text{transf}} = 0.33(6), \tag{18}$$

$$\text{Solution 2:} \quad P_{\text{dyn}} = 0.51(7), \quad P_{\text{transf}} = -0.33(7). \tag{19}$$

From the measurements the sign of both spin polarization components is known, P_{transf} is positive and P_{dyn} is negative (cf. Table III); thus solution 1 has to be the right one. Inserting the measured asymmetries $A_{\text{circ}} = -0.065(9)$ and $A_{\text{lin}} = 0.100(9)$ and the calculated P_{transf} and P_{dyn} of solution 1 into Eq. (11), we obtain

$$S_1 S_{\text{eff}} = -0.197(26) \quad \text{and} \quad S_3 S_{\text{eff}} = -0.197(38). \tag{20}$$

With the known degree of light polarization from optical measurements $S_1 = S_3 = 0.97(2)$ the polarization sensitivity of the Mott polarimeter is $S_{\text{eff}} = -0.202(27)$.

(iv) As a final step, we plot β, P_{transf}, and P_{dyn} in dependency on λ and δ_{45} in Fig. 4(c). The fact that all three curves cross each other in exactly one point is strong evidence for the internal consistency of the data. Furthermore the advantage of an overdetermined system is obvious: there is only one (λ, δ_{45}) pair which reproduces all three measured values at the same time, allowing only one solution to the problem.

The Hasylab data set [with $A_{\text{circ}}/A_{\text{lin}} = -0.53(20)$] yields the following matrix elements:

$$D_4 = 0.091(5), \quad D_5 = 0.049(6), \quad \delta_{45} = -0.97(10). \tag{21}$$

With $S_1 = S_3 = 0.99(1)$, this results in a Sherman function of $S_{\text{eff}} = -0.195(36)$. Throughout the present paper the value $S_{\text{eff}} = -0.20(3)$ is used.

The experimental matrix elements shown in Table IV are mean values of the two data sets [Eqs. (16) and (21)]. Theoretical matrix elements were not published; thus we derived them from the dynamical parameters of Ref. [38] by the same procedure applied to the experimental data. The comparison shows theoretical amplitudes that are too large which is due to the overestimated cross section. The phase differences agree very well. Since the measured quantities rely on the ratios and/or the squares of the matrix element amplitudes, we cannot determine the signs of D_4 and D_5; they are either both positive or negative.

TABLE IV. Theoretical and experimental amplitudes (in a.u.), and phase difference (in rad) of the dipole matrix elements for Xe $5p_{1/2}$ photoionization at 93.8 eV. The theoretical values were derived from the dynamical parameters.

		Theory[a]	Experiment
$5p^{-1}\,{}^2P_{1/2}$	D_4	0.098	0.092(3)
	D_5	0.053	0.047(3)
	δ_{45}	−1.03	−0.97(7)

[a]Frozen-core RRPA [38].

C. Xe 4*d* photoionization

The results of our measurements of the spin polarization, angular distribution, and fine-structure branching ratio are shown in Table V together with other experimental and theoretical data. The $4d$ partial cross section was determined by several authors [39,40,43,44]. In Ref. [44] the results of several experiments are compared and give a mean value of 21 Mb for 94-eV photon energy. Becker *et al.* [39] published data with the smallest uncertainties, thus we use their value of 20.5 Mb. The branching ratio was published by Yates *et al.* [45] and Ausmees *et al.* [46]. Interestingly their values differ somewhat [$\rho = 1.34(2)$ in the former and $\rho = 1.41(2)$ in the latter]; our own measurement gives 1.38(2) for 94 eV. The anisotropy parameter was published by Kämmerling and Schmidt [7] separately for both spin-orbit components (at 94.5 eV). Our own measurements give somewhat smaller values for both lines. The alignment A_{20} and orientation A_{10} of the ionic states were determined from angular distribution [7,47–50] and spin polarization [20] measurements of the Xe $N_{4,5}O_{2,3}O_{2,3}$ Auger electrons, respectively.

The Xe $4d$ photoionization process was also thoroughly investigated theoretically; relativistic [38,51–54] and nonrelativistic [55,56] RPA calculations were performed with frozen-core and relaxed ionic potentials. In the frozen-core model the charge distribution of the ion is taken to be static during photoionization, and the outgoing electron ''sees'' the frozen potential of the ionic core. This model works well for fast electrons, because they are not influenced by a rearrangement of the ion's charge distribution. Rearrangement is taken into account in the relaxed model mainly through a shielding of the hole by other electrons. In general, the relaxed model yields better results for slow electrons, because they are very sensitive to changes of the field they are moving in [56].

The authors of Refs. [38] and [55] published the dynamical parameters, whereas other authors published matrix elements from which the dynamical parameters in Table V were calculated using Eqs. (10), (A15–A20), (A29), and (A30). When comparing the experimental and theoretical data, it is important to take into account the deviations in the ionization thresholds. In the frozen-core RRPA calculations, the absolute values of Dirac-Hartree-Fock eigenvalues were used which lie 4.2 eV above the experimental thresholds. For this reason we used the frozen-core RRPA values at 98.0 eV photon energy. In the relaxed RRPA calculations the thresh-

TABLE V. Theoretical and experimental partial cross section σ, fine-structure intensity ratio $\rho(=\sigma_{5/2}/\sigma_{3/2})$, spin polarization components P_{transf} and P_{dyn}, angular anisotropy β, orientation A_{10}, and alignment A_{20} for Xe 4*d* photoionization at 93.8 eV.

		Theory				Experiment	
		frozen core RRPA[a]	frozen core RPAE[b]	relaxed RRPA[c]	relaxed RRPA overlap factors[d]	other	this work
4*d* Total	σ/Mb	28.1		20.7	19.1	20.5(1.0)[e]	
	ρ	1.36		1.35			1.38(2)
	β	0.34	0.36	0.25		0.27(4)[f]	
$4d^{-1}\,^2D_{5/2}$	σ/Mb	16.2 17.2[g]		11.9	10.9	11.9(6)[h]	
	P_{transf}	−0.54	−0.60[i]	−0.56	−0.56		−0.57(7)
	P_{dyn}	0.17	0.17[i]	0.12	0.12		0.15(5)
	β	0.34		0.24	0.275	0.35(1)[j]	0.23(4)
	A_{10}	−0.61[g]	−0.62	−0.61	−0.61		−0.65(15)[k]
	A_{20}	−0.24[g]	−0.24	−0.24	−0.24	−0.238(16)[l]	
$4d^{-1}\,^2D_{3/2}$	σ/Mb	11.9		8.8		8.6(4)[h]	
	P_{transf}	0.83	0.83	0.84			0.83(9)
	P_{dyn}	−0.24	−0.23	−0.13			−0.20(5)
	β	0.34		0.26		0.33(3)[j]	0.21(4)
	A_{10}		−0.61	−0.61			−0.58(13)[k]
	A_{20}		−0.22	−0.22		−0.22(3)[l]	

[a]Reference [38] at $h\nu=98.0$ eV; see text.
[b]Reference [55].
[c]Reference [52].
[d]Liu and Kelly (1992), cited in Ref. [7] as private communication; $h\nu=94.5$ eV.
[e]Reference [39].
[f]Reference [42].
[g]Reference [51] at $h\nu=98.0$ eV; see text.
[h]Calculated from σ and ρ.
[i]Calculated from the $^2D_{3/2}$ final state using the experimental branching ratio.
[j]Reference [7] at $h\nu=94.5$ eV.
[k]Reference [20].
[l]References [7,47].

old is taken as the difference between the self-consistent energies of the atomic and ionic ground states. These values differ by less than 1 eV from the experimental thresholds [54], and are not corrected. The matrix elements of Liu and Kelly are given only at 94.5 eV [7].

Similarly to the 5*s* and 5*p* ionization, the frozen-core RRPA calculations also overestimate the 4*d* partial cross section. Relaxation of the ionic core solves this problem and gives accurate values, but overlap integrals decrease σ too much. The influence of relaxation on the partial cross section for different photon energies was investigated in Refs. [53] and [54]. These authors found that including relaxation improves the agreement with experiment up to 100 eV, but at higher energies the agreement decreases. A similar behavior was found in Ref. [56] by comparing the frozen-core and relaxed versions of the RPAE theory.

A further discrepancy between the frozen-core and relaxed RRPA calculations can be found for the anisotropy parameter β and the dynamical spin polarization P_{dyn}. Unfortunately the measured dynamical polarization is between the two theoretical values. The transferred spin polarization P_{transf} alignment A_{20}, and orientation A_{10} are in very good agreement for all calculations and measurements.

A complete characterization of the 4*d* photoionization process in terms of dipole matrix elements is possible, because for each final ionic state there are five unknown quantities, three amplitudes and two phase differences [Eqs. (A13) and (A14)], and six measured values σ, A_{10}, A_{20}, P_{transf}, P_{dyn}, and β (Table V). A similar procedure to that in Sec. IV B was used to determine the matrix elements.

(i) First the three amplitudes were calculated analytically from σ, A_{10}, and A_{20}, using Eqs. (10) and (A29) or (A30). Since these equations contain only the squares of the amplitudes, their signs cannot be determined, and we rely on the signs of the theoretical values.

TABLE VI. Theoretical and experimental amplitudes (in a.u.) and phase differences (in rad) of the dipole matrix elements for Xe $4d$ photoionization at 93.8 eV. For the uncertainties of the phase differences, see Fig. 5. The right column shows the matrix elements with vanishing relativistic phase differences.

		Theory			Experiment		
		frozen core RRPA[a]	relaxed RRPA[b]	relaxed RRPA overlap factors[c]	other[d]	this work	this work
$4d^{-1}\,^2D_{3/2}$	D_1		0.078			$0.09^{+0.09}_{-0.02}$	0.087(17)
	D_2		0.036			$0.04^{+0.11}_{-0.03}$	0.044(32)
	D_3		0.428			$0.42^{+0.01}_{-0.06}$	0.421(10)
	δ_{12}		3.12			$3.6^{+1.3}_{-3.0}$	3.14(3)[e]
	δ_{23}		2.74			$2.3^{+1.8}_{-1.0}$	2.62(15)
$4d^{-1}\,^2D_{5/2}$	D_4	0.130	0.107	0.099	0.126(38)	$0.10^{+0.04}_{-0.01}$	0.115(10)
	D_5	0.130	0.107	0.103	0.125(22)	$0.11^{+0.01}_{-0.02}$	0.108(13)
	D_6	0.582	0.484	0.467	0.483(62)	$0.49^{+0.01}_{-0.02}$	0.482(10)
	δ_{45}	−0.80	−0.53	−0.57	±0.9(1.2)	$-0.68^{+0.24}_{-0.21}$	−0.59(11)
	δ_{56}	0.02	0.03	0.03	±0.1(1.2)	$0.35^{+0.32}_{-0.70}$	0.00(3)[e]

[a]Reference [51] at $h\nu = 98.0$ eV; see text.
[b]Reference [52].
[c]Liu and Kelly (1992), cited in Ref. [7] as private communication; $h\nu = 94.5$ eV.
[d]Reference [7] at $h\nu = 94.5$ eV.
[e]Values fixed to 3.14 ± 0.03 and 0.00 ± 0.03.

(ii) Using the amplitudes from (i), P_{transf}, P_{dyn}, and β were plotted in dependency on the two phase differences. For both final states all three curves cross each other approximately at one point, which roughly determines both phase differences.

(iii) To increase the precision a numerical optimization procedure was performed, using the amplitudes from (i) and the phase differences from (ii) as starting values. In this process the matrix elements were varied in order to minimize the squared difference between the measured and reproduced values expressed by the following equation:

$$Q = \left(\frac{A_{10} - A_{10,\mathrm{meas}}}{\Delta A_{10,\mathrm{meas}}}\right)^2 + \left(\frac{A_{20} - A_{20,\mathrm{meas}}}{\Delta A_{20,\mathrm{meas}}}\right)^2 + \left(\frac{\sigma - \sigma_{\mathrm{meas}}}{\Delta \sigma_{\mathrm{meas}}}\right)^2 + \left(\frac{\beta - \beta_{\mathrm{meas}}}{\Delta \beta_{\mathrm{meas}}}\right)^2 + \left(\frac{P_{\mathrm{transf}} - P_{\mathrm{transf,meas}}}{\Delta P_{\mathrm{transf,meas}}}\right)^2 + \left(\frac{P_{\mathrm{dyn}} - P_{\mathrm{dyn,meas}}}{\Delta P_{\mathrm{dyn,meas}}}\right)^2 . \quad (22)$$

The matrix elements obtained from the optimization procedure reproduce the measurements exactly. The results of this analysis are given in Table VI, in the second column from the right.

It is interesting to note that all the phase differences have large error bars. In Ref. [7] the situation is similar. This has several reasons. σ, A_{10}, and A_{20} are independent of the phases, and P_{transf} is only weakly dependent, i.e., these quantities do not contribute to the determination of the phase differences. The strongest dependency is on P_{dyn} [cf. Eqs. (A17) and (A20)], which is usually the most inaccurate due to the difficulty of determining the instrumental asymmetry of the Mott polarimeter. Furthermore, there is an ambiguity in the phase differences when they are used to reproduce the dynamical parameters within their error bars. This behavior is discussed in the next paragraph.

The uncertainties of the matrix elements, the three amplitudes, and two phase differences, cannot be adequately represented by simple one-dimensional bars. Rather we have to determine ranges in a five-dimensional space, within which the matrix elements reproduce the measured quantities within their uncertainties. We have carried this out by a systematic numerical variation of the former set of five parameters, checking compliance with the experimental values for each trial set. Results of this procedure for the two phase differences are presented in Fig. 5, while one-dimensional projections for the errors of the other parameters are shown in Table VI. These obviously represent an upper limit to the

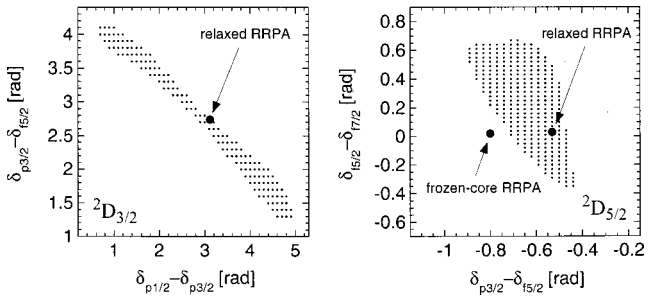

FIG. 5. Two-dimensional representation of pairs of phase difference values compatible with the measured data for both final states of the $4d$ photoionization. See the text for details.

TABLE VII. Theoretical and experimental amplitudes (in a.u) and phase differences (in rad) of the dipole matrix elements for Xe 4*d* photoionization at 93.8 eV in the nonrelativistic approximation. The left and middle columns were obtained from Table VI by using Eqs. (A21) and (A22). The right column is the result of a nonrelativistic analysis.

		Theory	Experiment	
		relaxed RRPA[a] (from Table VI)	this work (from Table VI)	this work (from nonrelat. analysis)
$4d^{-1}\,^2D_{3/2}$	D_p	0.087	0.095(19)	0.098(11)
	D_f	0.428	0.42(1)	0.420(8)
	δ_{pf}	−0.40	−0.52(15)	−0.54(13)
$4d^{-1}\,^2D_{5/2}$	D_p	0.107	0.115(10)	0.118(13)
	D_f	0.496	0.494(10)	0.494(10)
	δ_{pf}	−0.53	−0.59(11)	−0.60(14)

[a]Reference [52].

uncertainty of these parameters. Figure 5 is also very useful for a comparison with the theoretical phase differences. The results of the relaxed RRPA theory lie clearly within the shaded area for both final states, whereas the frozen-core value is outside the experimentally allowed area.

The overestimated partial cross section of the frozen-core RRPA theory is reflected by values of the amplitudes which are too large. The agreement between the amplitudes of both experiments and the relaxed RRPA theory is very good. Since all dynamical parameters except σ depend only on amplitude ratios, the discrepancy between the relaxed and frozen-core P_{dyn} and β is due to the difference in the nonrelativistic phase δ_{45}. This difference means that the changing ionic potential caused by relaxation influences the outgoing waves with different orbital angular momenta differently (l dependency). A dependence on j cannot be observed, since the relativistic phase vanishes in all calculations (π is equivalent to 0).

Since vanishing relativistic phases are compatible with the experimental results (cf. Fig. 5), we repeated our analysis with the conditions $\delta_{12}=3.14\pm0.03$ and $\delta_{56}=0\pm0.03$. The results of this analysis are in the right most column of Table VI. These matrix elements reproduce all the measured quantities perfectly. The amplitudes are practically the same as in the previous analysis, but the nonrelativistic phase differences are slightly altered. The fixing of one parameter reduces the error bars (determined as described above) substantially. There is an excellent agreement with the relaxed RRPA results of Ref. [52] for all ten parameters.

The transition to a completely nonrelativistic description of the 4*d* process in terms of matrix elements is given by Eqs. (A21) and (A22), and the results are shown in Table VII. Vanishing relativistic phase differences were already taken into account, but certain ratios of the amplitudes must also be fulfilled. The conditions $D_1/D_2=\sqrt{5}$ for the $^2D_{3/2}$ final state and $D_6/D_5=\sqrt{20}$ for the $^2D_{5/2}$ final state are met by both theoretical and experimental amplitudes (within the uncertainties). This means that the nonrelativistic approximation is valid in the present case.

In this way, we can also analyze our experiment using a nonrelativistic model as a starting point. The extraction of parameters then becomes similar to the case of the $5p_{1/2}$ photoionization, described above. Results for the matrix elements are given in Table VII, right column. Furthermore, we obtain $S_{\mathrm{eff}}=-0.20\pm0.02$ for the polarization sensitivity and $A_{10}=-0.59$ and $A_{20}=-0.23$ for the orientation and alignment, respectively. The excellent agreement of these values with those from the Auger electron measurements (Table V) proves the validity of the two-step model of Auger decay in the present case.

The validity of the nonrelativistic approximation can be also tested directly using the measured electron-spin polarizations. In the nonrelativistic approximation the spin polarizations of the two fine-structure components are related to each other; that is the spin polarization should vanish if the two components are not separated in the electron spectrometer [55]:

$$\rho P^{5/2}_{\mathrm{transf}}=-P^{3/2}_{\mathrm{transf}} \quad \text{and} \quad \rho P^{5/2}_{\mathrm{dyn}}=-P^{3/2}_{\mathrm{dyn}}. \tag{23}$$

These equations are fulfilled very well by our measurements for both P_{transf} and P_{dyn} (cf. Table V); thus the validity of the nonrelativistic approximation is confirmed. A detailed analysis of the Xe 4*d* photoionization process based on a modified nonrelativistic treatment was given in Ref. [9] for a broad photon energy range.

V. SUMMARY

We have presented a detailed study of Xe 4*d* inner-shell and Xe 5*s* and 5*p* valence-shell photoionization processes at 94-eV photon energy, close to the maximum of the 4*d* shape resonance. The use of advanced experimental techniques allowed us to perform spin-resolved electron spectroscopy with circularly and linearly polarized synchrotron radiation. For all three processes we measured two independent spin polarization components and the angular anisotropy parameter. These data were combined with published values of the cross section, anisotropy parameter, and intensity ratio of the fine-structure components. Additionally, for the 4*d* photoionization we used published values of the photoion align-

ment and orientation, which describe the polarization of the $4d^{-1}$ hole states.

The parameter sets we measured for the $5s$ and $5p_{1/2}$ photolines could be used to determine the instrumental asymmetry and the polarization sensitivity S_{eff} of our Mott polarimeter. For the $5p_{1/2}$ photoionization process a complete set of dipole matrix elements was also determined.

A combination of measurements on the $4d$ photolines with the calibration results from the $5s$ and $5p$ photolines made it possible to determine a complete set of relativistic dipole matrix elements independently for both final ionic states of the Xe $4d$ photoionization process. Detailed comparisons with theoretical calculations and other experimental data leads us to the following conclusions.

(i) A theoretical description of the valence photoionization processes by the frozen-core RRPA and RPAE models is good for all parameters, except for the partial cross section. The most important characteristic of these processes is that they are strongly influenced by the $4d$ shell (interchannel coupling).

(ii) In the case of the $4d$ ionization, where the results of both relaxed and frozen-core RRPA calculations are available, we found an excellent agreement between our data and the relaxed RRPA data for all photoionization parameters and matrix elements. This shows that at 94-eV photon energy relaxation plays a major role.

(iii) $4d$ photoionization can be described very well in the framework of a nonrelativistic approximation at this photon energy. This result is supported by both theoretical and experimental data in the form of extracted matrix elements, and also by spin polarization measurements. This finding is not unexpected, since relativistic effects should occur mainly in Cooper minima of the cross section.

An interesting subject for future investigations will be to examine the influence of relaxation and relativistic effects over a broad photon energy range. For this purpose spin polarization measurements should be performed especially in and around the cross section Cooper minima, and the corresponding theoretical results should be published.

ACKNOWLEDGMENTS

We would like to thank the BESSY and Hasylab staffs, especially T. Möller, for the excellent working conditions. We are thankful to D. Menke (Universität Bielefeld) for producing the multilayer and to F. Schäfers (BESSY) for testing it. We appreciate valuable discussions with B. Langer, B. Zimmermann, and G. Prümper during the course of this work. Financial support of the DFG is gratefully acknowledged (He 1049/7-1).

APPENDIX

The relationship between our measured quantities P_{transf}, P_{dyn}, and β, and the dipole matrix elements, were obtained using Eqs. (8) and (9) and the expressions given in Ref. [30]. They are given below for the photoionization of the Xe $4d$, $5s$, and $5p$ subshells. These formulas have the same forms for the photoionization of other closed-shell atoms. Expressions for the photoion polarization (orientation and alignment) are also given for the photoionization of d subshells.

1. Xe $5s$ photoionization

$$\text{Xe}\,5s^2\,5p^6(^1S_0)+h\nu\rightarrow \text{Xe}^+\,5s^1\,5p^6(^2S_{1/2})+e^-_{\text{Ph}}(\varepsilon p_{1/2},\varepsilon p_{3/2}),$$
$$k = 1 \quad 2. \tag{A1}$$

The index k is used to differentiate between the different final states, e.g., D_2 is the amplitude of the $\varepsilon p_{3/2}$ partial wave. The dynamical parameters are given by

$$\beta=\frac{D_2^2+\sqrt{8}D_1D_2\cos\delta_{12}}{D_1^2+D_2^2}, \tag{A2}$$

$$P_{\text{transf}}=\frac{D_1^2-D_2^2+\frac{\sqrt{2}}{2}D_1D_2\cos\delta_{12}}{D_1^2+\frac{5}{4}D_2^2+\frac{\sqrt{2}}{2}D_1D_2\cos\delta_{12}}, \tag{A3}$$

$$P_{\text{dyn}}=\frac{\frac{3}{\sqrt{2}}D_1D_2\sin\delta_{12}}{D_1^2+\frac{5}{4}D_2^2+\frac{\sqrt{2}}{2}D_1D_2\cos\delta_{12}}. \tag{A4}$$

In the nonrelativistic approximation there is only one outgoing p electron wave ($\delta_{12}=0$, $D_1=\sqrt{1/3}D_p$, and $D_2=\sqrt{2/3}D_p$) and all the dynamical parameters have fixed values: $\beta=2$ and $P_{\text{transf}}=P_{\text{dyn}}=0$.

2. Xe $5p$ photoionization

$$\mathrm{Xe}\,5s^2\,5p^6(^1S_0)+h\nu\rightarrow \mathrm{Xe}^+\,5s^2\,5p^5(^2P_{3/2})+e^-_{\mathrm{Ph}}(\varepsilon d_{5/2},\varepsilon d_{3/2},\varepsilon s_{1/2})$$

$$k = 1, \quad 2, \quad 3 \tag{A5}$$

$$\rightarrow \mathrm{Xe}^+\,5s^2\,5p^5(^2P_{1/2})+e^-_{\mathrm{Ph}}(\varepsilon d_{3/2},\varepsilon s_{1/2})$$

$$k = 4 \quad 5. \tag{A6}$$

The dynamical parameters are given by

$$\beta^{3/2}=\frac{4D_1^2-4D_2^2+6D_1D_2\cos\delta_{12}-2\sqrt{5}D_2D_3\cos\delta_{23}-6\sqrt{5}D_1D_3\cos\delta_{13}}{5(D_1^2+D_2^2+D_3^2)}, \tag{A7}$$

$$P^{3/2}_{\mathrm{transf}}=\frac{-9D_1^2+4D_2^2+5D_3^2+9D_1D_2\cos\delta_{12}-5\sqrt{5}D_2D_3\cos\delta_{23}}{12D_1^2+8D_2^2+10D_3^2+3D_1D_2\cos\delta_{12}-\sqrt{5}D_2D_3\cos\delta_{23}-3\sqrt{5}D_1D_3\cos\delta_{13}}, \tag{A8}$$

$$P^{3/2}_{\mathrm{dyn}}=\frac{-(15D_1D_2\sin\delta_{12}+3\sqrt{5}D_2D_3\sin\delta_{23}-6\sqrt{5}D_1D_3\sin\delta_{13})}{12D_1^2+8D_2^2+10D_3^2+3D_1D_2\cos\delta_{12}-\sqrt{5}D_2D_3\cos\delta_{23}-3\sqrt{5}D_1D_3\cos\delta_{13}}, \tag{A9}$$

$$\beta^{1/2}=\frac{D_4^2+\sqrt{8}D_4D_5\cos\delta_{45}}{D_4^2+D_5^2}=\frac{\lambda^2+\sqrt{8}\lambda\cos\delta_{45}}{\lambda^2+1}, \tag{A10}$$

$$P^{1/2}_{\mathrm{transf}}=\frac{D_4^2-D_5^2-\frac{\sqrt{2}}{2}D_4D_5\cos\delta_{45}}{D_5^2+\frac{5}{4}D_4^2+\frac{\sqrt{2}}{2}D_4D_5\cos\delta_{45}}=\frac{\lambda^2-1-\frac{\sqrt{2}}{2}\lambda\cos\delta_{45}}{1+\frac{5}{4}\lambda^2+\frac{\sqrt{2}}{2}\lambda\cos\delta_{45}}, \tag{A11}$$

$$P^{1/2}_{\mathrm{dyn}}=\frac{\frac{3}{\sqrt{2}}D_4D_5\sin\delta_{45}}{D_5^2+\frac{5}{4}D_4^2+\frac{\sqrt{2}}{2}D_4D_5\cos\delta_{45}}=\frac{\frac{3}{\sqrt{2}}\lambda\sin\delta_{45}}{1+\frac{5}{4}\lambda^2+\frac{\sqrt{2}}{2}\lambda\cos\delta_{45}}. \tag{A12}$$

A simplified form of the last three equations is also given using the ratio of the amplitudes $\lambda=D_4/D_5$.

3. Xe $4d$ photoionization

$$\mathrm{Xe}\,4d^{10}\,5s^2\,5p^6(^1S_0)+h\nu\rightarrow \mathrm{Xe}^+\,4d^9\,5s^2\,5p^6(^2D_{3/2})+e^-_{\mathrm{Ph}}(\varepsilon p_{1/2},\varepsilon p_{3/2},\varepsilon f_{5/2})$$

$$k = 1, \quad 2, \quad 3 \tag{A13}$$

$$\rightarrow \mathrm{Xe}^+\,4d^9\,5s^2\,5p^6(^2D_{5/2})+e^-_{\mathrm{Ph}}(\varepsilon p_{3/2},\varepsilon f_{5/2},\varepsilon f_{7/2})$$

$$k = 4, \quad 5, \quad 6. \tag{A14}$$

The dynamical parameters are given by

$$\beta^{3/2}=\frac{4}{5}\,\frac{-D_2^2+D_3^2-\frac{1}{2}\sqrt{5}D_1D_2\cos\delta_{12}-\frac{3}{2}\sqrt{5}D_1D_3\cos\delta_{13}+\frac{3}{2}D_2D_3\cos\delta_{23}}{D_1^2+D_2^2+D_3^2}, \tag{A15}$$

$$P^{3/2}_{\mathrm{transf}}=\frac{-5D_1^2-4D_2^2+9D_3^2+5\sqrt{5}D_1D_2\cos\delta_{12}-9D_2D_3\cos\delta_{23}}{10D_1^2+8D_2^2+12D_3^2-\sqrt{5}D_1D_2\cos\delta_{12}-3\sqrt{5}D_1D_3\cos\delta_{13}+3D_2D_3\cos\delta_{23}}, \tag{A16}$$

$$P_{\mathrm{dyn}}^{3/2}=\frac{-3\sqrt{5}(D_1D_2\sin\delta_{12}-2D_1D_3\sin\delta_{13}+\sqrt{5}D_2D_3\sin\delta_{23})}{10D_1^2+8D_2^2+12D_3^2-\sqrt{5}D_1D_2\cos\delta_{12}-3\sqrt{5}D_1D_3\cos\delta_{13}+3D_2D_3\cos\delta_{23}}, \tag{A17}$$

$$\beta^{5/2}=\frac{D_4^2-\frac{32}{7}D_5^2+\frac{25}{7}D_6^2-6\sqrt{\frac{2}{7}}D_4D_5\cos\delta_{45}-60\sqrt{\frac{2}{35}}D_4D_6\cos\delta_{46}+\frac{12}{7}\sqrt{5}D_5D_6\cos\delta_{56}}{5(D_4^2+D_5^2+D_6^2)}, \tag{A18}$$

$$P_{\mathrm{transf}}^{5/2}=\frac{\frac{3}{5}D_4^2+\frac{9}{35}D_5^2-\frac{6}{7}D_6^2-\frac{3}{5}\sqrt{\frac{7}{2}}D_4D_5\cos\delta_{45}+\frac{3}{7}\sqrt{5}D_5D_6\cos\delta_{56}}{\frac{21}{20}D_4^2+\frac{27}{35}D_5^2+\frac{33}{28}D_6^2-\frac{3}{10}\sqrt{\frac{2}{7}}D_4D_5\cos\delta_{45}-\frac{6}{10}\sqrt{\frac{10}{7}}D_4D_6\cos\delta_{46}+\frac{3}{35}\sqrt{5}D_5D_6\cos\delta_{56}}, \tag{A19}$$

$$P_{\mathrm{dyn}}^{5/2}=\frac{\frac{3}{\sqrt{14}}D_4D_5\sin\delta_{45}-6\sqrt{\frac{2}{35}}D_4D_6\sin\delta_{46}+\frac{3}{\sqrt{5}}D_5D_6\sin\delta_{56}}{\frac{21}{20}D_4^2+\frac{27}{35}D_5^2+\frac{33}{28}D_6^2-\frac{3}{10}\sqrt{\frac{2}{7}}D_4D_5\cos\delta_{45}-\frac{6}{10}\sqrt{\frac{10}{7}}D_4D_6\cos\delta_{46}+\frac{3}{35}\sqrt{5}D_5D_6\cos\delta_{56}}. \tag{A20}$$

In the nonrelativistic approximation using

$$^2D_{3/2}:\quad \delta_{12}=\pm\pi,\quad \delta_{23}=\delta_{pf}+\pi,\quad D_1=\sqrt{5/6}D_p,\quad D_2=\sqrt{1/6}D_p,\quad D_3=D_f, \tag{A21}$$

$$^2D_{5/2}:\quad \delta_{45}=\delta_{pf},\quad \delta_{56}=0,\quad D_4=D_p,\quad D_5=\sqrt{1/21}D_f,\quad D_6=\sqrt{20/21}D_f \tag{A22}$$

Eqs. (A15)–(A20) are reduced to

$$\beta^{3/2}=\frac{4D_f^2+D_p^2-12\sqrt{3/2}D_fD_p\cos\delta_{fp}}{5(D_f^2+D_p^2)}, \tag{A23}$$

$$P_{\mathrm{transf}}^{3/2}=\frac{6D_f^2-6D_p^2+\sqrt{6}D_fD_p\cos\delta_{fp}}{8D_f^2+7D_p^2-2\sqrt{6}D_fD_p\cos\delta_{fp}}, \tag{A24}$$

$$P_{\mathrm{dyn}}^{3/2}=\frac{-5\sqrt{6}D_fD_p\sin\delta_{fp}}{8D_f^2+7D_p^2-2\sqrt{6}D_fD_p\cos\delta_{fp}}, \tag{A25}$$

$$\beta^{5/2}=\frac{4D_f^2+D_p^2-12\sqrt{3/2}D_fD_p\cos\delta_{fp}}{5(D_f^2+D_p^2)}, \tag{A26}$$

$$P_{\mathrm{transf}}^{5/2}=\frac{-4D_f^2+4D_p^2-2\sqrt{2/3}D_fD_p\cos\delta_{fp}}{8D_f^2+7D_p^2-2\sqrt{6}D_fD_p\cos\delta_{fp}}, \tag{A27}$$

$$P_{\mathrm{dyn}}^{5/2}=\frac{-10\sqrt{2/3}D_fD_p\sin\delta_{fp}}{8D_f^2+7D_p^2-2\sqrt{6}D_fD_p\cos\delta_{fp}}. \tag{A28}$$

Orientation A_{10} and alignment A_{20} for photoionization processes leading to $^2D_{3/2}$ and $^2D_{5/2}$ final states of the photoion are given by [57,58]

$$A_{10}^{3/2}=\frac{S_3}{2\sqrt{5}}\frac{5D_1^2+2D_2^2-3D_3^2}{D_1^2+D_2^2+D_3^2},\qquad A_{20}^{3/2}=\frac{(-2)}{10}\frac{5D_1^2-4D_2^2+D_3^2}{D_1^2+D_2^2+D_3^2}, \tag{A29}$$

$$A_{10}^{5/2}=\frac{S_3}{2}\left(\frac{3}{35}\right)^{1/2}\frac{7D_4^2+2D_5^2-5D_6^2}{D_4^2+D_5^2+D_6^2}, \tag{A30}$$

$$A_{20}^{5/2}=\frac{(-2)}{5\sqrt{14}}\frac{7D_4^2-8D_5^2+\frac{5}{2}D_6^2}{D_4^2+D_5^2+D_6^2}.$$

A_{20} is given here with respect to the direction of the electric field vector **E** of linearly polarized radiation.

In the nonrelativistic approximation using Eqs. (A21) and (A22), A_{10} and A_{20} are given by

$$A_{10}^{3/2}=\frac{3S_3}{4\sqrt{5}}\frac{3\lambda^2-2}{1+\lambda^2},\quad A_{20}^{3/2}=-\frac{1}{10}\frac{2+7\lambda^2}{1+\lambda^2}, \tag{A31}$$

$$A_{10}^{5/2}=\frac{S_3}{2}\left(\frac{7}{15}\right)^{1/2}\frac{3\lambda^2-2}{1+\lambda^2},\quad A_{20}^{5/2}=-\frac{1}{5}\sqrt{\frac{2}{7}}\frac{2+7\lambda^2}{1+\lambda^2}, \tag{A32}$$

with $\lambda=D_p/D_f$. In this case orientation and alignment can be expressed solely with the ratio of the dipole amplitudes.

[1] M. Y. Amusia and M. Kutzner, in *VUV- and Soft X-Ray Photoionization*, edited by U. Becker and D. A. Shirley (Plenum, New York, 1996).

[2] D. J. Kennedy and S. T. Manson, Phys. Rev. A **5**, 227 (1972).

[3] J. W. Cooper, Phys. Rev. **128**, 681 (1962).

[4] J. W. Cooper, Phys. Rev. Lett. **13**, 762 (1964).

[5] U. Becker and D. A. Shirley, in *VUV- and Soft X-ray Photoionization* (Ref. [1]).

[6] B. Kämmerling and V. Schmidt, Phys. Rev. Lett. **67**, 1848 (1991); W. R. Johnson, K. T. Cheng, B. Kämmerling, and V. Schmidt, *ibid.* **69**, 1144 (1992).
[7] B. Kämmerling and V. Schmidt, J. Phys. B **26**, 1141 (1993).
[8] S. J. Schaphorst, Q. Qian, B. Krässig, P. V. Kämpen, N. Scherer, and V. Schmidt, J. Phys. B **30**, 4003 (1997).
[9] G. Snell, B. Langer, M. Drescher, N. Müller, B. Zimmermann, U. Hergenhahn, J. Viefhaus, U. Heinzmann, and U. Becker, Phys. Rev. Lett. **82**, 2480 (1999).
[10] U. Heinzmann and N. A. Cherepkov, in *VUV- and Soft X-ray Photoionization* (Ref. [1]).
[11] A. Hausmann, B. Kämmerling, H. Kossmann, and V. Schmidt, Phys. Rev. Lett. **61**, 2669 (1988).
[12] B. Schmidtke, M. Drescher, N. A. Cherepkov, and U. Heinzmann, J. Phys. B **33**, 2451 (2000).
[13] T. J. Gay and F. B. Dunning, Rev. Sci. Instrum. **63**, 1635 (1992).
[14] P. Elleaume and J. Chavanne, Nucl. Instrum. Methods Phys. Res. A **304**, 719 (1991).
[15] M. Drescher, G. Snell, U. Kleineberg, H.-J. Stock, N. Müller, U. Heinzmann, and N. B. Brookes, Rev. Sci. Instrum. **68**, 1939 (1997).
[16] N. Müller, R. David, G. Snell, R. Kuntze, M. Drescher, N. Böwering, P. Stoppmanns, S.-W. Yu, U. Heinzmann, J. Viefhaus, U. Hergenhahn, and U. Becker, J. Electron Spectrosc. Relat. Phenom. **72**, 187 (1995).
[17] G. Snell, M. Drescher, N. Müller, U. Heinzmann, U. Hergenhahn, J. Viefhaus, F. Heiser, U. Becker, and N. B. Brookes, Phys. Rev. Lett. **76**, 3923 (1996).
[18] J. B. Kortright, H. Kimura, V. Nikitin, K. Mayama, M. Yamamoto, and M. Yanagihara, Appl. Phys. Lett. **60**, 2963 (1992).
[19] J. Viefhaus, L. Avaldi, G. Snell, M. Wiedenhöft, R. Hentges, A. Rüdel, F. Schäfers, D. Menke, U. Heinzmann, A. Engelns, J. Berakdar, H. Klar, and U. Becker, Phys. Rev. Lett. **77**, 3975 (1996).
[20] G. Snell, M. Drescher, N. Müller, U. Heinzmann, U. Hergenhahn, and U. Becker, J. Phys. B **32**, 1 (1999).
[21] O. Björneholm, F. Federmann, C. Larsson, U. Hahn, A. Rieck, S. Kakar, and T. Möller, Rev. Sci. Instrum. **66**, 1732 (1995).
[22] Hasylab Annual Report (1994), p. 24.
[23] W. Peatman, C. Carbone, W. Gudat, W. Heinen, P. Kuske, J. Pfluger, F. Schäfers, and T. Schröter, Rev. Sci. Instrum. **60**, 1445 (1989).
[24] BESSY Annual Report (1987), p. 371.
[25] K. Rabinovitch, L. R. Canfield, and R. P. Madden, Appl. Opt. **4**, 1005 (1965).
[26] A. Gaupp and M. Mast, Rev. Sci. Instrum. **60**, 2213 (1989).
[27] T. Koide, T. Shidara, M. Yuri, N. Kandaka, K. Yamaguchi, and H. Fukutani, Nucl. Instrum. Methods Phys. Res. A **308**, 635 (1991).
[28] L. G. Gray, M. W. Hart, F. B. Dunning, and G. K. Walters, Rev. Sci. Instrum. **55**, 88 (1984).
[29] U. Heinzmann, J. Phys. B **13**, 4353 (1980); **13**, 4367 (1980).
[30] K.-N. Huang, Phys. Rev. A **22**, 223 (1980).
[31] M. Born and E. Wolf, *Principles of Optics* (Pergamon, New York, 1970).
[32] C. Heckenkamp, F. Schäfers, G. Schönhense, and U. Heinzmann, Z. Phys. D **2**, 257 (1986).
[33] U. Fano, Phys. Rev. **178**, 131 (1969); Phys. Rev. **184**, 250 (1969).
[34] E. G. Berezhko and N. M. Kabachnik, J. Phys. B **10**, 2467 (1977).
[35] H. Klar, J. Phys. B **13**, 4741 (1980).
[36] N. M. Kabachnik and O. V. Lee, J. Phys. B **22**, 2705 (1989).
[37] A. Fahlman, T. A. Carlson, and M. O. Krause, Phys. Rev. Lett. **50**, 1114 (1983).
[38] K.-N. Huang, W. R. Johnson, and K. T. Cheng, At. Data Nucl. Data Tables **26**, 33 (1981).
[39] U. Becker, D. Szostak, H. G. Kerkhoff, M. Kupsch, B. Langer, R. Wehlitz, A. Yagishita, and T. Hayaishi, Phys. Rev. A **39**, 3902 (1989).
[40] J. B. West, P. R. Woodruff, K. Codling, and R. G. Houlgate, J. Phys. B **9**, 407 (1976).
[41] M. O. Krause, T. A. Carlson, and P. R. Woodruff, Phys. Rev. A **24**, 1374 (1981).
[42] L. Torop, J. Morton, and J. B. West, J. Phys. B **9**, 2035 (1976).
[43] U. Becker, T. Prescher, E. Schmidt, B. Sonntag, and H.-E. Wetzel, Phys. Rev. A **33**, 3891 (1986).
[44] B. Kämmerling, H. Kossman, and V. Schmidt, J. Phys. B **22**, 841 (1989).
[45] B. W. Yates, K. H. Tan, L. L. Coatsworth, and G. M. Bancroft, Phys. Rev. A **31**, 1529 (1985).
[46] A. Ausmees, S. J. Osborne, R. Moberg, S. Svensson, S. Aksela, O.-P. Sairanen, A. Kivimaki, A. N. D. Brito, E. Nommiste, J. Jauhiainen, and H. Aksela, Phys. Rev. A **51**, 855 (1995).
[47] S. Southworth, U. Becker, C. M. Truesdale, P. H. Kobrin, D. W. Lindle, S. Owaki, and D. A. Shirley, Phys. Rev. A **28**, 261 (1983).
[48] B. Kämmerling, B. Krässig, and V. Schmidt, J. Phys. B **23**, 4487 (1990).
[49] B. Kämmerling, Ph.D. thesis, Universität Freiburg, 1991.
[50] G. Snell, E. Kukk, B. Langer, and N. Berrah, Phys. Rev. A **61**, 042709 (2000).
[51] W. R. Johnson, K. T. Cheng, B. Kämmerling, and V. Schmidt, Phys. Rev. Lett. **69**, 1144 (1992).
[52] W. R. Johnson and K. T. Cheng, Phys. Rev. A **46**, 2952 (1992).
[53] Z. Altun, M. Kutzner, and H. P. Kelly, Phys. Rev. A **37**, 4671 (1988).
[54] M. Kutzner, V. Radojevic, and H. P. Kelly, Phys. Rev. A **40**, 5052 (1989).
[55] N. A. Cherepkov, J. Phys. B **12**, 1279 (1979).
[56] M. Y. Amusia, V. K. Ivanov, and L. V. Chernysheva, Phys. Lett. A **59**, 191 (1976).
[57] V. Schmidt, Rep. Prog. Phys. **55**, 1483 (1992).
[58] U. Hergenhahn, Ph.D. thesis, Technical University Berlin, 1996.